Water-extractable organic matter from tropical soils and biochar-amended tailors the colloidal behavior of nanoparticles mitigating their toxicity through molecular eco-corona formation

Laís G. Fregolente[1,2*], João Vitor dos Santos[2], Gabriela H. Da Silva[1], Theodoro da R. Salles[1,3], Simone G. S. dos Santos[1], Luelc S. Costa[1], Gabriela A. Nogueira[4], Márcia C. Bisinoti[4], Carlos A. Pérez[5], Patrick G. Hatcher[2], Iseult Lynch[6] and Diego Stéfani T. Martinez[1,3*]

[1]Brazilian Nanotechnology National Laboratory (LNNano), Brazilian Center for Research in Energy and Materials (CNPEM), Campinas, Sao Paulo, Brazil

[2]Department of Chemistry and Biochemistry, Old Dominion University (ODU), Norfolk, Virginia, United States of America

[3]School of Technology, University of Campinas (UNICAMP), Limeira, Sao Paulo, Brazil

[4]Laboratory of Environmental Sciences Studies (LECA), Department of Chemistry and Environmental Sciences (DQCA), Institute of Biosciences, Letters and Exact Sciences (IBILCE), São Paulo State University (UNESP), São José do Rio Preto, São Paulo, Brazil

[5]Brazilian Synchrotron Light Laboratory (LNLS), Brazilian Centre for Research in Energy and Materials (CNPEM), Campinas, Sao Paulo, Brazil

[6]School of Geography, Earth and Environmental Sciences (GEES), University of Birmingham (UoB), Edgbaston, Birmingham, United Kingdom

*Corresponding author

E-mail addresses: lais.fregolente@lnnano.cnpem.br; diego.martinez@lnnano.cnpem.br

Supporting Information (SI)

Abbreviation List

^{1}H-NMR: ^{1}H Nuclear Magnetic Resonance

µ-XRF: Micro-X-ray fluorescence

ADE: Amazonian Dark Earth

ADEC: ADE cold-water extraction

ADEH: ADE hot-water extraction

AgNPs: Silver nanoparticles

AI: Aromatic index

B: Biochar

BC: Biochar cold-water extraction

BH: Biochar hot-water extraction

CC: Complexation capacity

CCC: Critical coagulation concentration

ConAC: Condensed aromatic carbon

CONCORDIA: Core consistency diagnostic

CL: Total ligand site concentration

Cryo-TEM: Cryogenic transmission electron microscopy

CuO: Copper oxide

CuONP: Copper oxide nanoparticles

DBE: Double bond equivalent

D_h: Hydrodynamic diameter

DOC: Dissolved organic carbon

DOM: Dissolved organic matter

DRX: X-ray diffraction

EC_{50}: Effective concentration

EEM: Excitation-emission matrix mode

FET: Fish Embryo Toxicity

FTIR: Fourier transform infrared spectroscopy

hpf: Hours post-fertilization

K: Conditional stability constant

LC_{50}: Letal concentration

NOM: Natural organic matter

NP: Nanoparticle

OECD: Organization for Economic Co-operation and Development

PARAFAC: Parallel factor analysis

PtNMs: Platinum nanomaterials

SOM: Soil organic matter

S: Oxisol

SC: Oxisol cold-water extraction

SB: Oxisol-Biochar system

SH: Oxisol hot-water extraction

SBC: SB cold-water extraction

SBH: SB hot-water extraction

SEM: Scanning electron microscopy

$SUVA_{254}$: Specific ultraviolet absorbance at 254nm

TGA: Thermogravimetric analysis

TEM: Transmission electron microscopy

TOC: Total organic carbon

UPW: ultrapure water

WEOM: Water extractable organic matter

XPS: X-ray photoelectron spectroscopy

ZHE_1: Zebrafish Hatching Enzyme 1

SECTION 1: Biochar Characterization

X-ray diffraction (XRD)

The crystalline structure of the samples was evaluated by X-ray diffraction (D8 Advance ECO, Bruker) using CuKα radiation (λ = 1,5406 Å), in the range of 10-90° (2θ), with a step size of 0.04° and an accumulation time of 0.6 s per step.

Thermogravimetric analysis (TGA)

Ash content was determined by thermogravimetric analysis (STA 449 F3, Netzsch), using a heating ramp of 20 to 850 °C at 10 °C/min.

Raman spectroscopy

Raman spectra were recorded using a 532 nm circular laser line as the excitation source, and a 50x objective lens for focusing the laser on the sample surface (XploRA Plus, Horiba). Acquisition parameters included 1% filter, 50 μm slit, 10 accumulations, and a 30 s acquisition time. The intensity ratio of the D and G bands (I_D/I_G) was calculated using deconvoluted vibrational modes of the G band (~1580 cm^{-1}) and the D band (~1350 cm^{-1}). Deconvolution was performed using Origin 2022b (OriginLab Corporation), and the values represent the average of three spectra.

Fourier Transform Infrared Spectroscopy (FTIR)

FTIR spectra were obtained in the mid-infrared region (Cary 600 Series, Agilent Technologies) in the range of 4000–400 cm^{-1}, with a resolution of 16 cm^{-1}, and with 128 scans. Solid samples were dispersed in KBr prior to analysis and then pressed to form the pellets.

X- ray photoelectron spectroscopy (XPS)

XPS measurements were performed by applying Al Kα X-rays (K-Alpha, Thermo Scientific). Survey spectra (full-range) were acquired to identify the elemental composition with a spatial resolution of 400 μm and a pass energy of 50.0 eV. High-resolution spectra were recorded for C (C 1s) analyzed with Thermo Avantage software (version 5.957, ThermoFisher, Basingstoke).

Measurement parameters included: a total acquisition time of 2 min 23.3 seconds, 15 scans, spot size of 400 μm, standard lens mode, constant analyzer energy (CAE) with a pass energy of 50.0 eV, energy step size of 0.100 eV, and 191 energy steps.

Results and Discussion

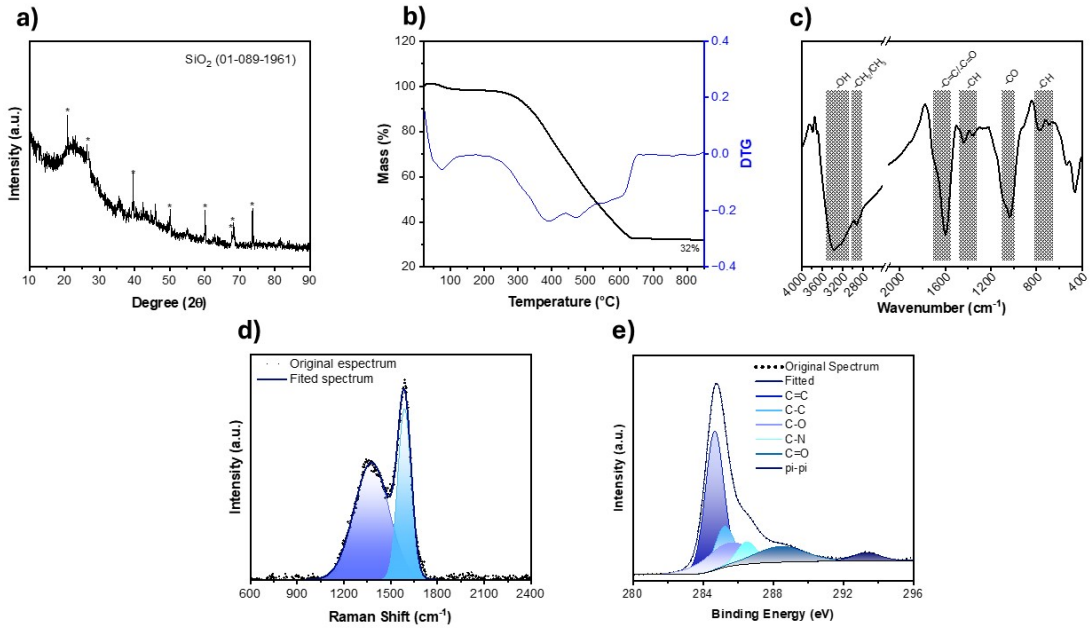

Figure S1. Biochar characterization by a) X-ray diffraction (XRD), b) thermogravimetric analysis (TGA), c) Fourier transform infrared spectroscopy (FTIR), d) Raman spectroscopy, and e) C1s X-ray photoelectron spectroscopy (XPS).

Biochar from sugarcane bagasse characterization is shown in Figure S1. The diffraction pattern of biochar shows a large peak between 15 and 35° (2θ), with a maximum at approximately 22–24° (2θ) (Fig. S1a)[1,2]. This profile is attributed to the low structural ordering of biochar, characteristic of carbonaceous material from biomass processed through pyrolysis at low temperatures. Further, it reveals a pattern of SiO_2 (PDF#01-089-1961) related with quartz phase, agreeing with the ash content (32%) observed in TGA analysis [3] (Fig. S1b).

Further, the Raman spectrum data confirms the low-structured profile of biochar indicated by the intense band at 1568 cm^{-1}, related with O-moieties, and the band at 1370 cm^{-1}, of lower intensity, indicating the graphitization degree. The I_D/I_G ratio of 0.68 suggests defects in the biochar chemical structure, with small aromatics domains[3,4]. Different vibration modes were observed in FTIR spectrum and identified as: -OH stretching (3363 cm^{-1}), -CH_2/CH_3 stretching (2916 cm^{-1}), C=C/C=O stretching (1710-592 cm^{-1}), -CH bending (1436,1350, 771, and 684 cm^{-1}), -CO stretching (1050 cm^{-1})[2,5]. The high content of functional groups is also in agreement with XPS C 1s high resolution, indicating the presence of C-O, C-N, and C=O bonds on the material's surface.

SECTION 2: Soil Characterization

Thermogravimetric analysis (TGA)

Ash content was determined using thermogravimetric analysis (STA 449 F3, Netzsch), heating the sample from 20 to 850 °C at a rate of 10 °C/min.

Results and Discussion

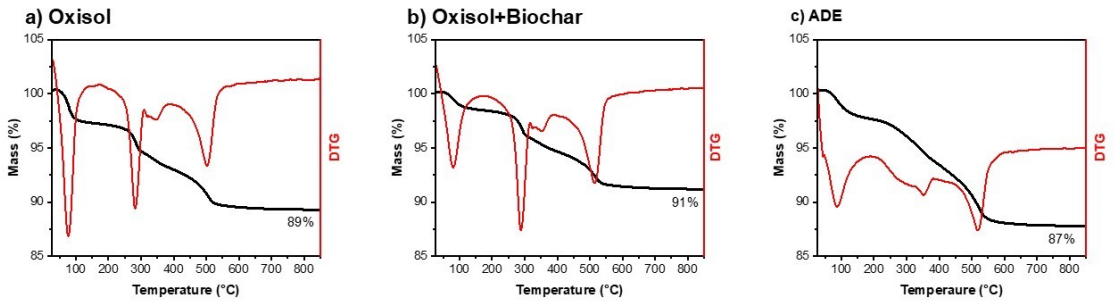

Figure S2. TGA of a) Oxisol, b) Oxisol-Biochar system, and c) Amazonian Dark Earth (ADE). DTG – Derivative Thermogravimetric curve – is the first derivative of the TGA curve, and represents the rate of change of mass with respect to temperature.

The thermal stability of soils and Oxisol amended with biochar was assessed through thermogravimetric analysis, also used to determine their ash content. The ash content in the samples was 87% in ADE, 89 % in Oxisol, and 91% in Oxysol-Biochar system. This indicates that the addition of biochar to Oxisol increased the soil ash content, what is probably due to the ash content in the biochar (32%, please see Fig. S1, Section 1). Even though the biochar addition to Oxisol was low (0.5 % w/w), silicates were identified in the biochar composition (please see Fig. S1, Section1), and it probably contributed to increase the ash percentage. Despite the ash content, the profile of thermogravimetric curves of Oxisol and Oxisol+Biochar system were similar, showing three main mass loss events, where the first one is associated to adsorbed water (~80°C), and the other two, at ~300°C and ~500°C, are related to the loss of organic matter of labile and more recalcitrant structure, respectively.

The thermogravimetric curve of ADE samples presented also three mass loss events, where the first one was related to adsorbed water (~80°C). Further, the thermogravimetric curve showed less defined thermal events and a shift to higher temperatures, which was more pronounced to the second mass loss event (~350°C), indicating the presence of more complex/stable organic structures in ADE soil composition, requiring higher temperatures to be eliminated.

SECTION 3: CuO Nanoparticle Characterization

Results and Discussion

CuONP morphology assessed by TEM revealed a quasi-spherical shape, with an average diameter of 6.79±0.22 nm. DLS measurements indicated a hydrodynamic diameter of 125.37±2.07 nm. The crystalline structure evaluated by XRD indicated a single-phase CuONP (JCPDS 01-089-5898). The peaks at binding energies around 934.7 eV and 954.5 eV could be assigned to the Cu $2p_{3/2}$ and Cu $2p_{1/2}$ peaks of CuO, respectively, and satellite peaks of Cu $2p_{3/2}$ around 942.0 eV and of $Cu2p_{1/2}$ at 963.0 eV, characteristics of Cu^{2+}, confirm the formation of CuONP[6,7] (Fig. S3).

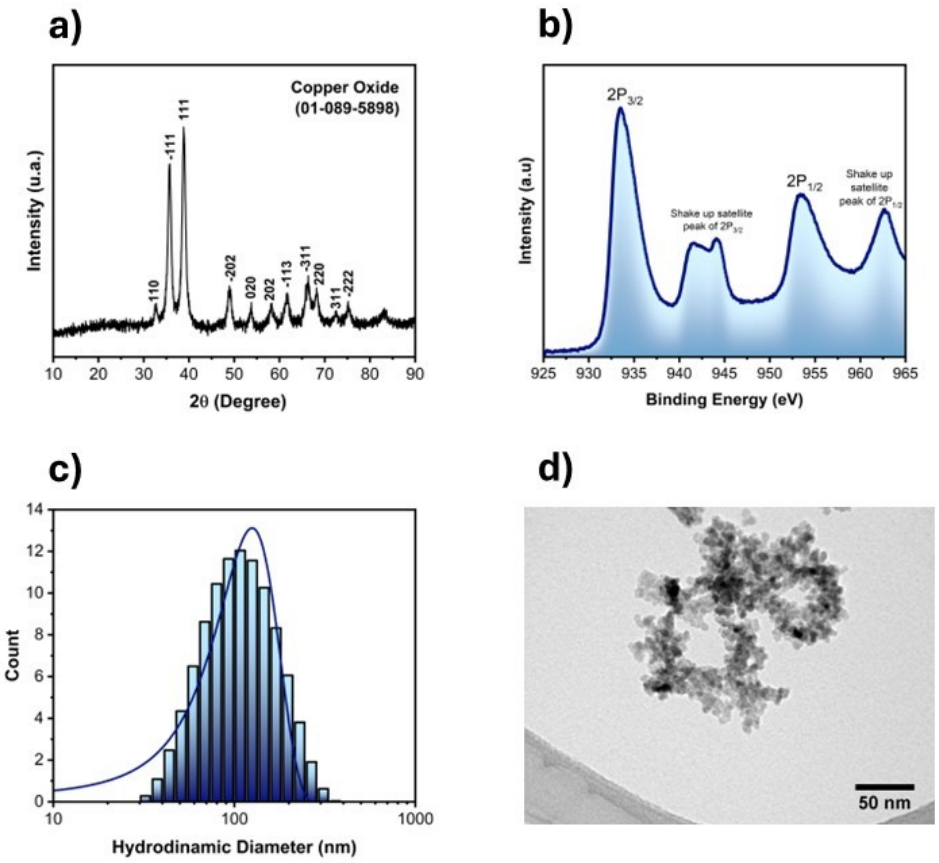

Figure S3. Copper oxide nanoparticle characterization by a) X-ray diffraction (XRD), b) X- ray photoelectron spectroscopy (XPS), c) hydrodynamic diameter, and d) transmission electron microscopy (TEM).

SECTION 4: Water Extractable Organic Matter (WEOM) Characterization

Fourier Transform Infrared Spectroscopy (FTIR)

The spectra were acquired for WEOM extracted from Amazonian Dark Earth (ADE) soil under cold water or hot water conditions (samples labeled ADEC and ADEH, respectively), and Biochar extracted with cold and hot water (labelled BC and BH, respectively). The WEOMs were freeze-dried, and the powders were dispersed in KBr (previously dried in an electric oven at 40 °C for 60 min) for pellet preparation. The spectra were obtained in the mid-infrared region (FTIR) (Cary 600 Series, Agilent Technologies) in the range of 4000–400 cm^{-1}, with a resolution of 16 cm^{-1}, and 128 scans.

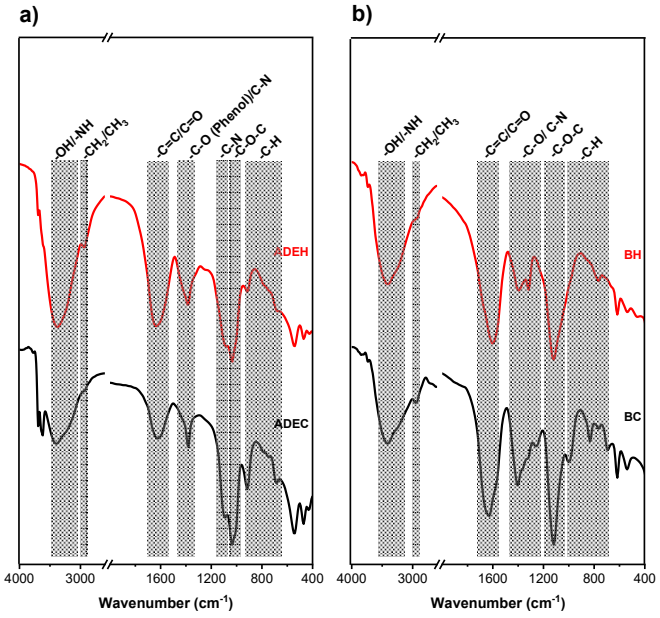

Figure S4. FTIR spectra of WEOM from a) Amazonian Dark Earth (ADE) and b) biochar (B) from cold- (C) and hot- (H) water extractions.

Ultraviolet-visible spectroscopy (UV-Vis) and dissolved organic carbon (DOC)

Results and Discussion

Table S1 shows the concentration of DOC, the absorbance ratios E_2/E_3 and E_4/E_6, as well as the specific UV absorbance at 254nm ($SUVA_{254}$) for the water-extractable organic matter (WEOM) extracted from Oxisol, Oxisol-Biochar system, Amazonian Dark Earth (ADE) soil, and biochar through cold- and hot-extraction. $SUVA_{254}$ (L mg^{-1} m^{-1}) was used to estimate the aromaticity at 254 nm and it was normalized according to the extracted DOC concentrations (mg C L^{-1}) (Equation 1) [8,9].

$$SUVA254 = \frac{\frac{A_{254}}{d}}{DOC} \quad (1)$$

Where A_{254} is the absorbance at 254 nm, and d is the optical path of the cuvette (m).

A positive correlation of DOC extracted with temperature was observed for soil samples and biochar. Hot-water extraction showed higher values of DOC in the WEOMs compared to cold-water extractions (Table S1). The spectroscopic indices are used as indicator of the molecular structure and composition of WEOM. The E_2/E_3 ratio can be indicative of molecular size and aromaticity, where the higher the value, the lower the molecular size and aromaticity, associated with less complex structures; for E_4/E_6, higher values indicate aromatic structures with low condensation, associated with labile compounds, i.e., easier to degrade or transform. Higher temperature preferentially mobilized labile carbon structures such as carbohydrates and fulvic acids, which is consistent with the decrease of $SUVA_{254}$ values and E_4/E_6 ratio trends (Table S1)[10–12]. A positive correlation of DOC extracted with temperature was observed for soil samples and biochar. The higher the values of $SUVA_{254}$, the higher the content of aromatic compounds in the samples, while lower values are associated with simple structural compounds. Hot-water extraction showed higher values of DOC in the WEOMs compared to cold-water extractions (Table S1). Higher temperature preferentially mobilized labile carbon structures such as carbohydrates and fulvic acids, which is consistent with the decrease of $SUVA_{254}$ values and E_4/E_6 ratio trends (Table S1)[10–12]. The solubility of organic carbon could be linked to many factors such as microbial biomass, where temperature could contribute to higher extractions [13], and clay content, considering that the organic carbon extractability of clay soil is less sensitive to temperature [14], which can affect the evaluation of carbon content and the composition of the water-extracts [10,15].

Table S1. Dissolved organic carbon (DOC) concentration, E_2/E_3 and E_4/E_6 absorbance ratios, and specific UV absorbance (SUVA) at 254 nm of dissolved organic matter extracted from Oxisol, Oxisol-Biochar system, Amazonian Dark Earth, and biochar from cold- and hot-water extraction.

Sample		**DOC**	**UV-Vis**		
		mg C L^{-1}	**E_2/E_3**	**E_4/E_6**	**$SUVA_{254}$** (L mg C^{-1} m^{-1})
Oxisol (S)	SC	13.3	2.083	1.000	1.67
	SH	45.6	3.119	1.030	0.87
Oxisol+Biochar system (SB)	SBC	8.6	2.079	1.063	2.74
	SBH	56.1	2.925	1.152	0.85
Biochar (B)	BC	168.0	3.327	2.824	3.37
	BH	386.4	3.245	4.080	3.00
Amazonian Dark Earth (ADE)	ADEC	60.8	1.978	1.723	3.25

ADEH	351.2	4.266	2.136	1.29

*The addition of "C" and "H" after the sample label means the temperature employed in the water extraction process, where "C" is used for cold-water extraction and "H" for hot-water extraction.

Excitation-emission matrix fluorescence spectroscopy (EEM-Fluorescence)

Results and Discussion

EEM-Fluorescence was used to qualitatively estimate the difference in the organic composition among the WEOM from different origins. EEMs-fluorescence data revealed similar overall compositions among soil and biochar spectra, showing a main peak at [λ_{Ex}220/ λ_{Em}425] and a secondary peak at [λ_{Ex}325/ λ_{Em}425], attributed to fulvic acids or humic-like acids of small size and complexity[16–19]. However, the soils' spectrum presented a low intensity peak at [λ_{Ex}200/ λ_{Em}300], associated with aliphatic and low complexity compounds such as carbohydrates and simple aromatic proteins (e.g. tyrosine-like), and a peak at [λ_{Ex}280/ λ_{Em}350] related to soluble microbial-like products containing aromatic proteins (e.g., tryptophan) and amino sugars[19–22]. Other quality indices such as fluorescence index (FI) [23] and the humification index (HIX) (i.e., the degree of condensation of aromatic structures) [24] (Fig. S6) were used to distinguish the organic matter source and its chemical reactivity, respectively. Values of FI (the area at λ_{Em} 435–480 nm divided by the area at λ_{Em}300–345 nm, at λ_{Ex} 254 nm) lower than 1.5 are generally related to terrestrial sources (allochthonous), while higher values are linked to the microbial source (autochthonous) [23,25,26]. The HIX (the ratio of fluorescence emission intensity λ_{Em} 450 nm and λ_{Em} 500 nm at an excitation wavelength of λ_{Ex} 370 nm) is related to the presence of condensed aromatic structures in the samples [24–27]. These values are presented in Table S1 and can be valuable indicators of changes to the composition of WEOM as a result of increasing the temperature of the water used for extraction and following biochar addition to soil.

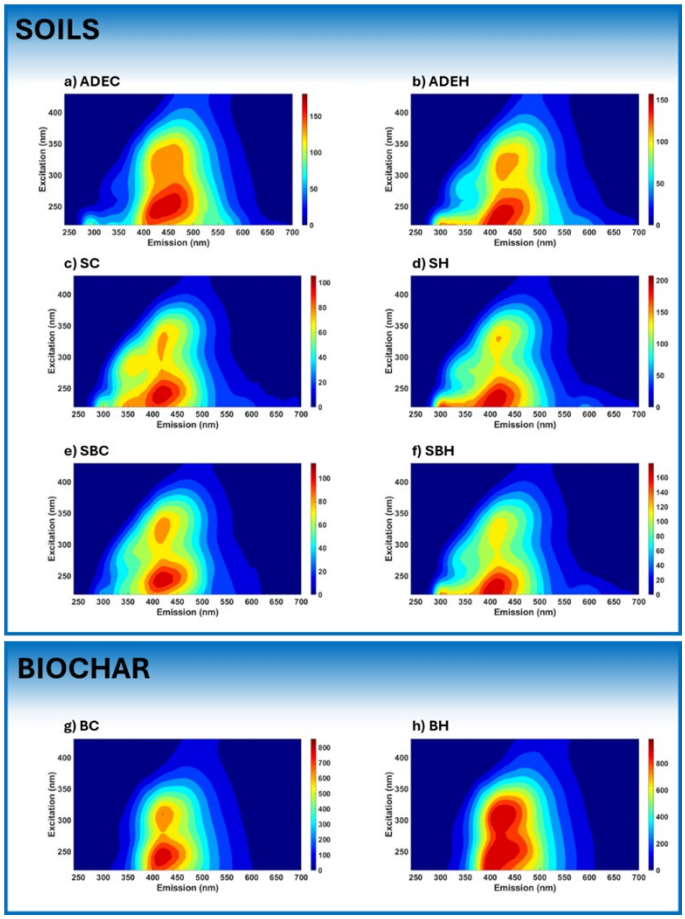

Figure S5. Excitation-Emission matrix (EEM) spectra of WEOM from cold- and hot-water extraction of Amazonian Dark Earth (samples ADEC and ADEH), Oxisol (SC, SH), Oxisol-Biochar system (SBC, SBH), and biochar (BC< BH) where C in the name indicates cold extraction while H implies hot-water extraction.

EEMs-fluorescence data revealed similar overall compositions between ADE and biochar samples (Fig. S5), both indicative of an allochthonous C source based on their lower fluorescence index (FI) values [28–30] (Fig. S6). As biochar was obtained from sugarcane pyrolysis, and ADE organic matter primarily originates from above-ground plant litter residues, their lower FI values reflect the allochthonous profile of their organic matter [28–30] (Fig. S6). The humification index (HIX) decreased following hot-water extraction, which preferentially mobilized simpler compounds such as carbohydrates and fulvic acids [10–12]. The increase in WEOM's DOC value with temperature is not linked to the degree of humification (HIX), as higher temperatures of extraction are associated with labile carbon structures, which is consistent with $SUVA_{254}$ values and E_4/E_6 ratio (Table S1) [10–12]. Further, the DOC enhancement can be due to nitrogen-rich compounds such as amino acids and amino sugars, favored in hot-water extractions [15].

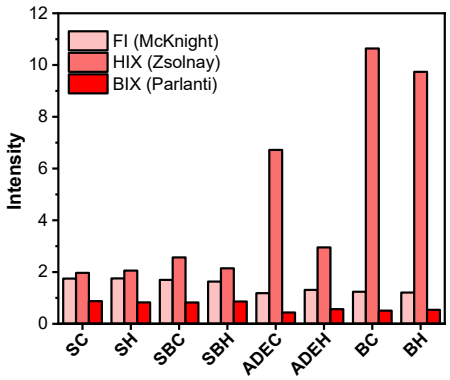

Figure S6. Fluorescence indices, such as Fluorescence Index (FI, by McKnight), Humification Index (HIX, by Zsolnay), and Microbial Material (BIX, by Parlanti), obtained by PARAFAC of WEOM extracted from ADE, biochar, Oxisol, and Oxisol-Biochar system.

Proton nuclear magnetic resonance (^{1}H-NMR)

WEOM samples were diluted with deuterated water (D_2O, Acros Organics, 100% D) to achieve a solution with a ratio of 90% H_2O to 10% D_2O. Sodium 2,2,3,3-tetradeutero-3-trimethylsilylpropanoate (TSP, Acros Organics, 98% D) was added at a concentration of 0.83 µM as an internal reference. One-dimensional ^{1}H NMR spectra were recorded using a modified water suppression pulse sequence (PEW5shapepr). The acquisition parameters included a 4 s relaxation delay, a time domain of 16 k, and 1024 scans. Spectra were normalized to DOC content. Spectral integration was performed over the chemical shifts corresponding to different ^{1}H chemical environments: aliphatic protons (C**H**3, 0.6-1.0 ppm; C**H**2, 1.0-1.4 ppm; **H**C−C−C-X, where X is a heteroatom such as O, N, or S, 1.4-1.85 ppm), protons in the α position to double bonds (**H**C−C=Y, 1.85-3.2 ppm), protons attached to oxygenated carbons (**H**C-OR, 3.2-4.4 ppm), olefinic protons (**H**C=R, 5.0-6.5 ppm), aryl protons on aromatic rings (**H**-Ar, 6.5-8.3 ppm), and protons in carbonyl groups (**H**C=O, 8.3-10.0 ppm). The ^{1}H signal between 4.4 and 5.0 ppm was not considered due to attenuation by the water suppression pulses. While the region from 0.0 to 0.6 ppm ("methane" region) was measured for normalization to total spectral intensity, it was not evaluated in this manuscript. Resonances in this region are typically due to dissolved methane [31] or poorly characterized silicates [32], and were excluded from interpretation due to their unclear context in DOM. Sharp singlet peaks indicative of pure compounds were observed for protons in acetic acid/acetate (1.9-2.1 ppm), methanol (3.2-3.4 ppm), and formic acid (8.1-8.3 ppm) in some spectra. Signals from these regions were summed and reported as low molecular weight compounds and subtracted from their respective regions. Integrals were converted to a carbon basis using the H/C ratios expected for the detected protons [33]. Each integral was then normalized to the total spectral intensity. Results are shown in Table S2.

Table S2. Relative distribution of carbon across functional groups in WEOM from ADE and biochar, estimated from ^{1}H-NMR data using H/C correlation. ADE – Amazonian Dark Earth, B – Biochar, C – cold-water extraction, H – hot-water extraction.

Functional Group (ID)		^{1}H-NMR Chemical Shift (ppm)	ADEC	ADEH	BC	BH
O=CH		8.3-10.0	1.3%	1.6%	2.9%	3.5%
Aromatic		6.5-8.3	7.0%	7.3%	17.8%	20.8%
Olefin		5.0-6.5	2.2%	2.1%	2.6%	3.6%
HC-O-R		3.2-4.4	31.1%	43.5%	21.7%	26.1%
HC-C=Y		1.85-3.2	18.7%	20.1%	27.9%	27.1%
Aliphatic	CH	1.4-1.85	9.7%	7.3%	9.3%	7.3%
	CH_2	1.0-1.4	22.4%	9.6%	12.1%	8.1%
	CH_3	0.6-1.0	6.9%	8.3%	4.6%	3.0%

Aliphatic	39.1%	25.2%	26.0%	18.4%
Oxygenated	51.1%	65.2%	52.5%	56.7%
Olefin	2.2%	2.1%	2.6%	3.6%
Aromatic	7.0%	7.3%	17.8%	20.8%

Electrospray ionization Fourier transform ion cyclotron resonance mass spectrometry (ESI-FT-ICR-MS)

The powdered WEOM samples were solubilized in ultrapure water, sonicated for 10 min, and then batch treated with cation-exchange resin (Dowex 50WX8 100–200 mesh, Acros Organics). Samples were diluted in methanol (Fisher Scientific, Optima LC-MS grade) to result in a 1:1 MeOH:water solution. Analyses were carried out using a 10 Tesla Bruker Daltonics Apex Qe FT-ICR spectrometer with an Apollo II electrospray ionization (ESI) source (Bruker, USA). Samples were injected at 120 $\mu L\ hr^{-1}$ and analyzed in negative-ion mode, (-)ESI. The instrument was calibrated externally with polyethylene glycol [34], and the tune validation was made using Suwannee River Fulvic Acid [35]. A total of 300 scans were accumulated across a mass range of 200 – 1000 Da for each sample. Procedural blanks were analyzed between samples to ensure no carryover effects. ESI voltages and ion accumulation delays were optimized for each sample to ensure consistent spraying and harmonize the number of detected species of each sample. Once mass spectra were acquired, peaks with signal-to-noise ratios ≥ 3 were selected, and the mass lists were internally calibrated using naturally abundant fatty acids, dicarboxylic acids, and CH_2-homologous series [36]. Peaks that appeared in process blanks were removed, along with salt, doubly charged, and isotopologue (^{13}C) peaks [37]. Empirical formulas were assigned to peaks using C, H, O, N, S, and P elements in the range of $^{12}C_{5-\infty}$, $^{1}H_{5–100}$, $^{16}O_{1–30}$, $^{14}N_{0–5}$, $^{32}S_{0–4}$, and $^{31}P_{0–2}$. Only formulas within ± 1 ppm error were chosen for the final formula lists. Formulas that did not stick to established molecular rules for natural organic matter were excluded from consideration. For mass peaks with ambiguous assignments (meaning they could match multiple molecular formulas), a refinement process was carried out by considering their inclusion within homologous series such as CH_2, H_2, COO, CH_2O, C_2H_4O, O, H_2O, and NH_3. Ultimately, only one molecular formula was selected for each mass peak in the final formula list for each sample.

Molecular catalogs were explored by calculating key metrics indicative of structural properties: molecular weight; number of double bond equivalents (DBE) - number of double bonds or cyclization in a molecule; and modified aromaticity index (AI_{mod}) – a indicative of the double-bond density in a molecule. For $AI_{mod} \geq 0.67$ molecules are condensed aromatic compounds (ConAC); for $0.67 > AI_{mod} \geq 0.50$ molecules are aromatic compounds with aliphatic side chains; and formulas with AI_{mod} =0.00 are viewed as fully saturated compounds. Molecular formulas were also categorized based on 1) the presence of non-O heteroelements: CHO, CHON, CHOS, and CHOP, and 2) compound class they could represent: condensed aromatic compounds, ConAC ($AI_{mod} \geq 0.67$); lignin ($AI_{mod} < 0.67$; $H/C < 1.5$; $0.1 > O/C < 0.67$); tannin ($H/C < 1.5$; $O/C \geq 0.67$; $AI_{mod} < 0.67$); sulfonic acid ($H/C \geq 2.0$ $O/C < 0.67$; $S > 0$); sugar ($H/C \geq 1.5$; $O/C \geq 0.55$; $N > 0$); protein ($H/C \geq 1.5$; $O/C < 0.55$; $N > 0$); lipid ($H/C \geq 1.5$; $O/C < 0.67$; $N=0$), and unsaturates ($H/C <1.5$; $0 > AImod < 0.67$; $O/C <0.1$) [36,37]. Molecular formulas were visualized on van Krevelen diagrams [38].

The numbers of identified molecular formulae determined by negative ion mode ESI were 2826 formulas for ADEC and 1736 formulas for ADEH, showing 1160 similar formulas between them. For biochar, 1695 formulas were identified for BC and 1187 formulas for BH, with 1039 being common formulas present in both biochar extracts.

Table S3. Relative percentage of compounds' formulas identified by ESI-FT-ICR-MS on the WEOM samples of ADE and biochar.

Compound Classes	ADEC	ADEH	BC	BH
			(%)	
CHO	67.08	81.73	95.85	98.52
CHON	18.60	6.86	0.54	0.66
CHOS	13.92	11.41	3.61	0.82
CHOP	0.40	-	-	-
ConAC-like	9.28	1.36	18.54	19.74
Lignin-like	55.95	59.68	69.58	74.44
Tannin-like	13.41	22.09	5.33	3.10
Sulfonic Acid-like	10.62	0.55	3.5	0.36
Sugar-like	4.43	11.61	2.03	1.57
Protein-like	3.15	3.45	0.15	-
Lipid-like	3.04	1.27	0.84	0.78
Unsaturated-like	0.07	-	0.03	-
Extra-like	0.05	-	-	-
AI	0.38	0.35	0.53	0.56
DBE	11.80	12.55	16.22	15.90

(-) Not identified; AI: aromatic index; DBE: Double bond equivalent.

SECTION 5: Eco-corona Characterization

EEM-PARAllel FACtor analysis

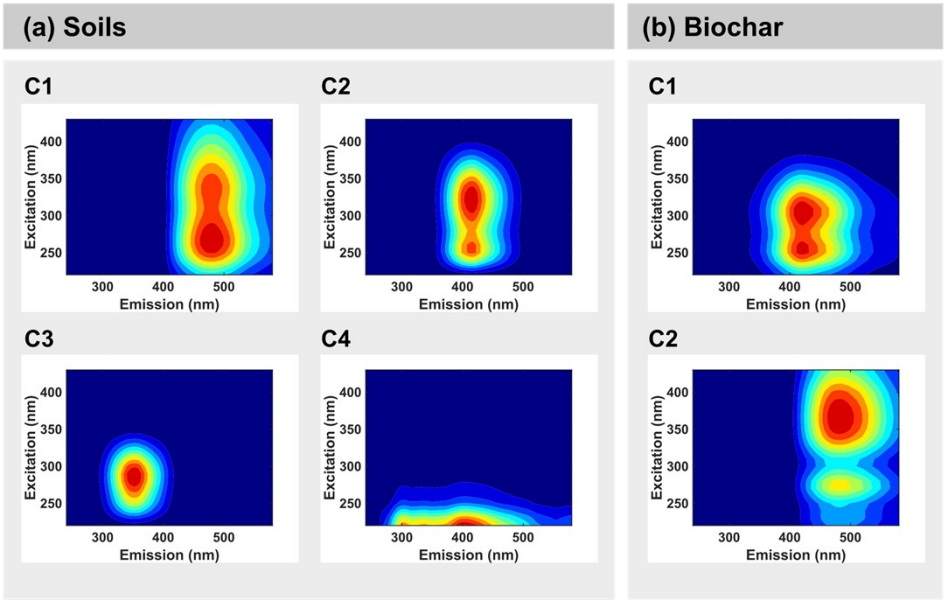

Figure S7. PARAFAC-identified components representing interactions between soil WEOM and CuONPs: (a) WEOM from Oxisol, Oxiso-Biochar system, and Amazonian Dark Earth, where C1, C2, and C3 were identified as the main components, and C4 was likely noise-related signal; (b) WEOM from biochar alone, being identified two components (C1 and C2).

Fourier Transform Infrared Spectroscopy (FTIR): The main functional groups present in the molecules comprising the eco-corona acquired by CuONP upon interaction with WEOM were attributed by FTIR analysis. The spectra were obtained in the mid-infrared region (FTIR) (Cary 600 Series, Agilent Technologies) in the range of 4000–400 cm^{-1}, with a resolution of 16 cm^{-1}, and 128 scans, with the solid samples being dispersed in KBr. The KBr was previously dried in an electric oven at 40 °C for 60 min, thoroughly mixed with the sample, and then pressed to form the pellet.

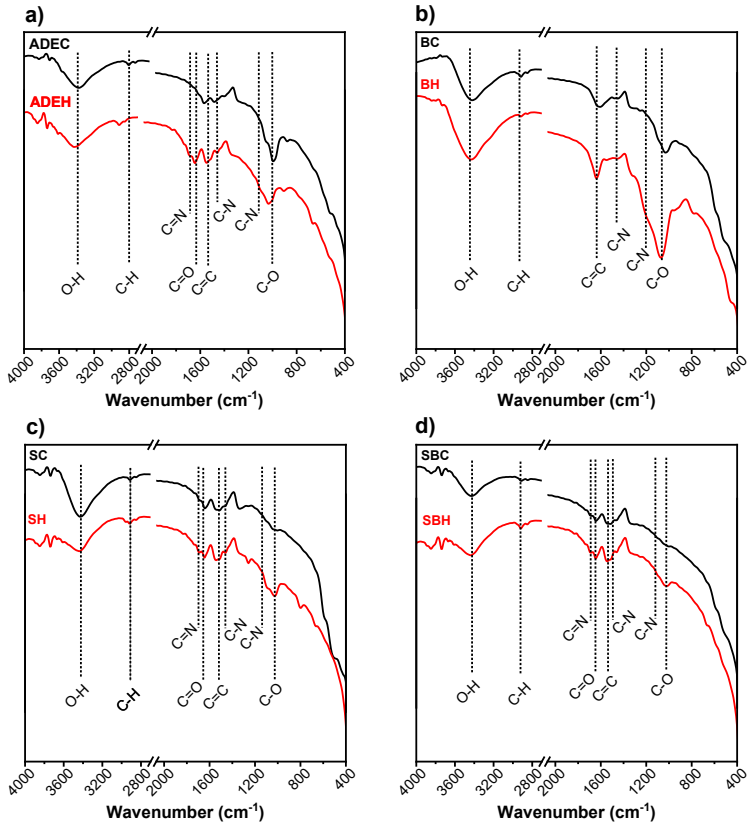

Figure S8. FTIR spectra of CuONP with hard corona of WEOM from a) Amazonian Dark Earth (ADE), b) biochar, c) Oxisol, and d) Oxisol-Biochar system, after three washing steps with UPW.

X- ray photoelectron spectroscopy (XPS)

XPS measurements were performed applying Al Kα X-rays (K-Alpha, Thermo Scientific). Survey spectra (full-range) were acquired to identify the elemental composition with a spatial resolution of 400 µm and a pass energy of 50.0 eV. High-resolution spectra were recorded for C (C 1s). The spectra were analyzed with Thermo Avantage software (version 5.957, ThermoFisher, Basingstoke).

Measurements parameters included: a total acquisition time of 2 min 23.3 seconds, 15 scans, spot size of 400 µm, standard lens mode, constant analyzer energy (CAE) with a pass energy of 50.0 eV, energy step size of 0.100 eV, and 191 energy steps.

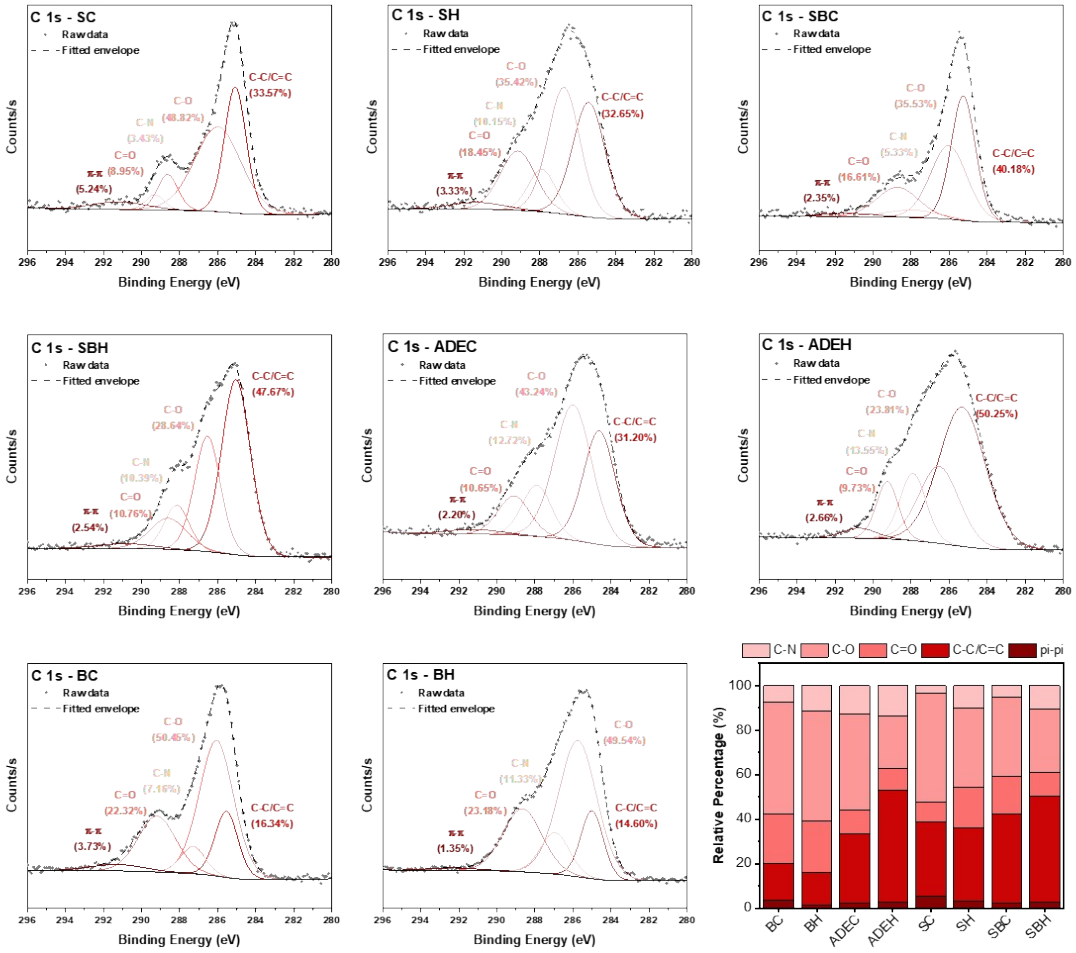

Figure S9. XPS carbon (C1s) spectra for CuONP with hard corona obtained from nanoparticle interaction with WEOM from Oxisol, Oxisol-Biochar system, Amazonian Dark Earth and biochar, after three wash steps with UPW, and the relative percentage of chemical bonds obtained from the relative peak intensities.

Cryo-transmission electron microscopy (Cryo-TEM)

Cryo-TEM was used to identify the eco-corona formation on CuONPs primarily for those samples that presented better results from quenching titration, i.e., WEOM samples from hot-water extraction. Thus, Figure S10 presents the images of SH and SBH samples where no eco-corona formation was identified. The images resemble those of CuONP in UPW (Fig. 2a), where no difference in contrast surrounding the nanoparticles is identified, which would otherwise indicate the presence of a molecular layer (eco-corona) adhered to the nanoparticle surface. Images of WEOM from cold-water extraction were obtained only for samples where quenching titration and stability results showed outstanding behavior such as higher binding affinities (log K and CC values) and aggregation inhibition from NaCl addition, i.e., ADEC and BC samples (Fig. 2b and 2c).

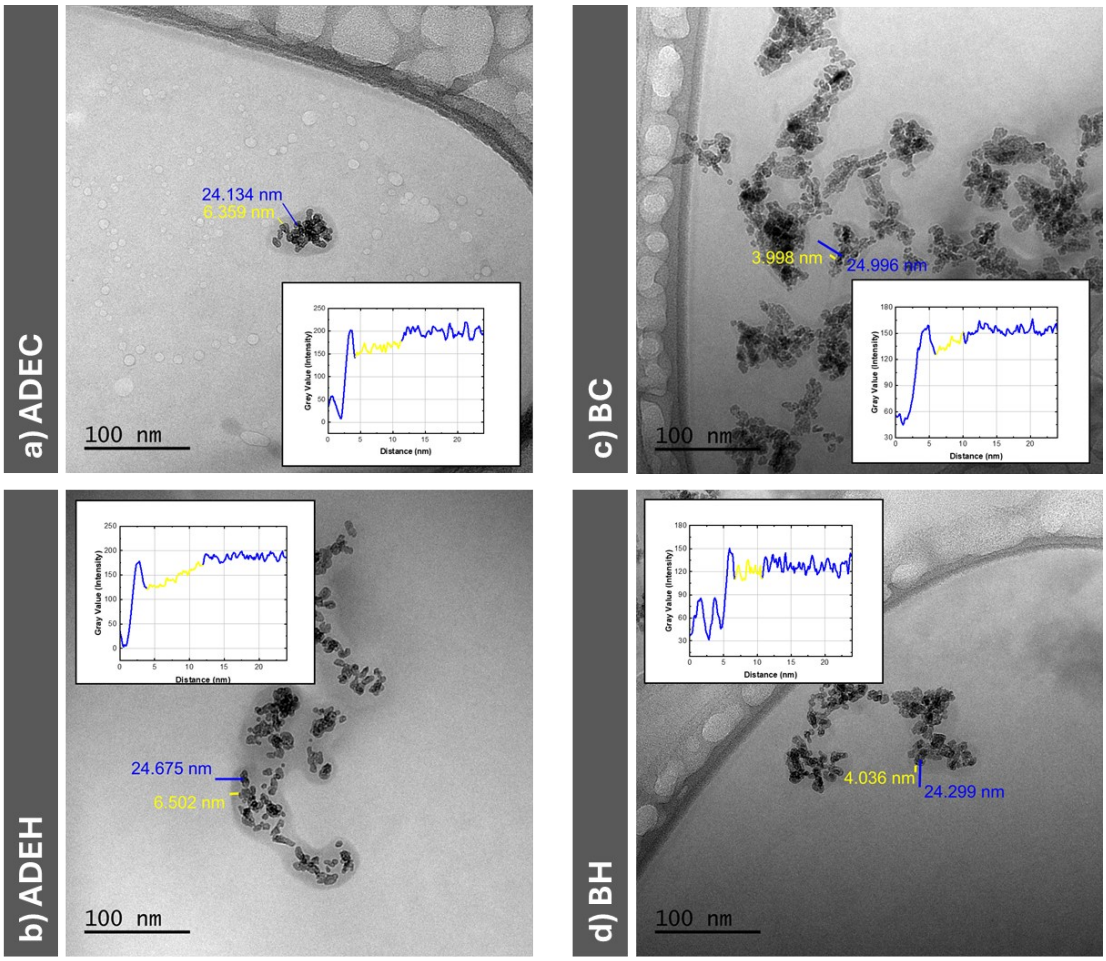

Figure S10. Cryo-TEM images of eco-corona identification on CuONP from their interaction with WEOM samples (ADEC, ADEH, BC, and BH) to estimated corona thickness, measured by contrast differentiation, represented by yellow colored lines in the grey value (intensity) versus distance (nm) plots.

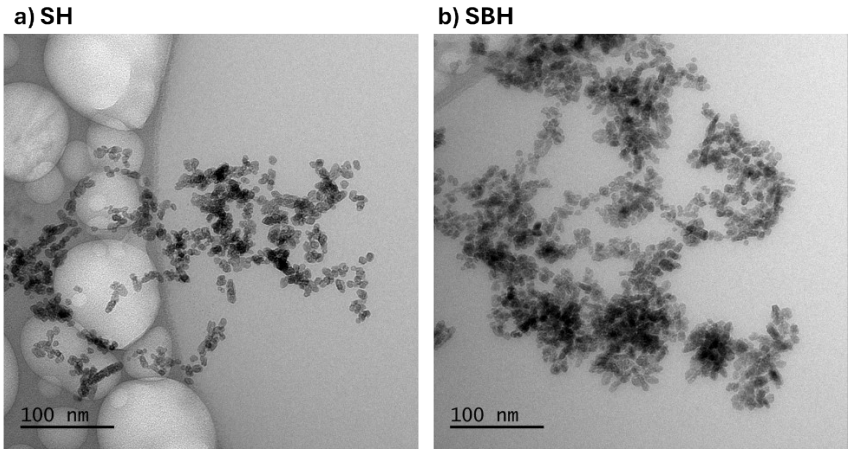

Figure S11. Cryogenic transmission electron microscopy images of CuONP interaction with WEOM from a) SH and b) SBH samples.

SECTION 6: Nanoparticle and WEOM Interaction

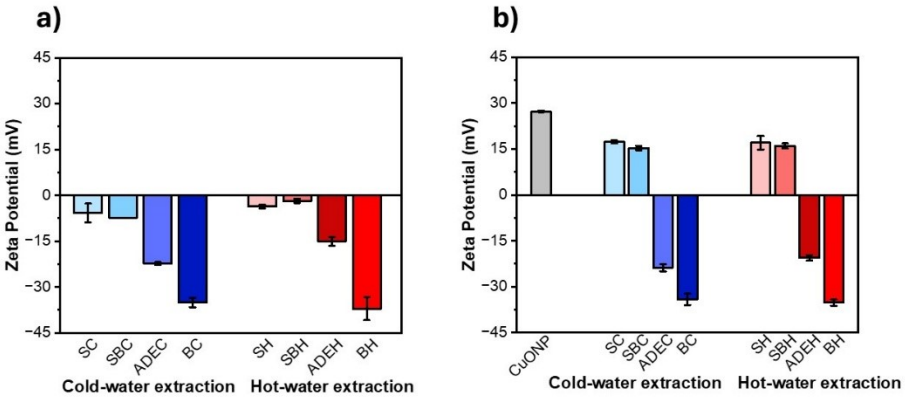

Figure S12. a) Zeta potential for WEOM samples from hot- and cold-water extractions; b) Zeta potential of CuONP in UPW and after WEOM addition. S – Oxisol, SB – Oxisol-Biochar system, ADE – Amazonian Dark Earth, with C and H indicating cold- and hot-water extractions, respectively.

Aggregation Kinetics

Determination of attachment efficiency

The aggregation slope is divided into two phases that are used to determine the attachment efficiency. The first one corresponds to when the aggregation rate constant (k) is defined as the period from the experimental initiation (t_0) and is known as reaction-limited aggregation (RLA). At this point the D_h increases with time, and it corresponds to the period from the initial aggregation (D_{h0}) to the time that D_h reaches values that exceeded at least 1.50 of the initial D_{h0}. The second one is known as diffusion-limited aggregation (DLA), where the aggregation rate constant (k_{fast}) is independent of electrolyte concentration and aggregate formation occurs rapidly. During DLA the diffusion rate controls the aggregation process. The k value is calculated following Equation 2 (E2)

$$k = \frac{1}{N_0}\left(\frac{dD_t(t)}{dt}\right)_{t\to 0} \qquad \text{(E2)}$$

where N_0 is the initial particle concentration. The attachment efficiency (α) is determined by normalizing the constant of the initial slope (RLA) (k), of the aggregation profile, by the constant under favorable aggregation conditions (k_{fast}) (DLA) for each solution chemistry, as described by Equation 3 [39–41].

$$\alpha = \frac{k}{k_{fast}} = \frac{\frac{1}{N_0}\left(\frac{dD_t(t)}{dt}\right)_{t\to 0}}{\frac{1}{N_{0fast}}\left(\frac{dD_h(t)}{dt}\right)_{t\to 0fast}} \qquad \text{(E3)}$$

All the measurements for each NaCl concentration, and all the tested media, were acquired in duplicate.

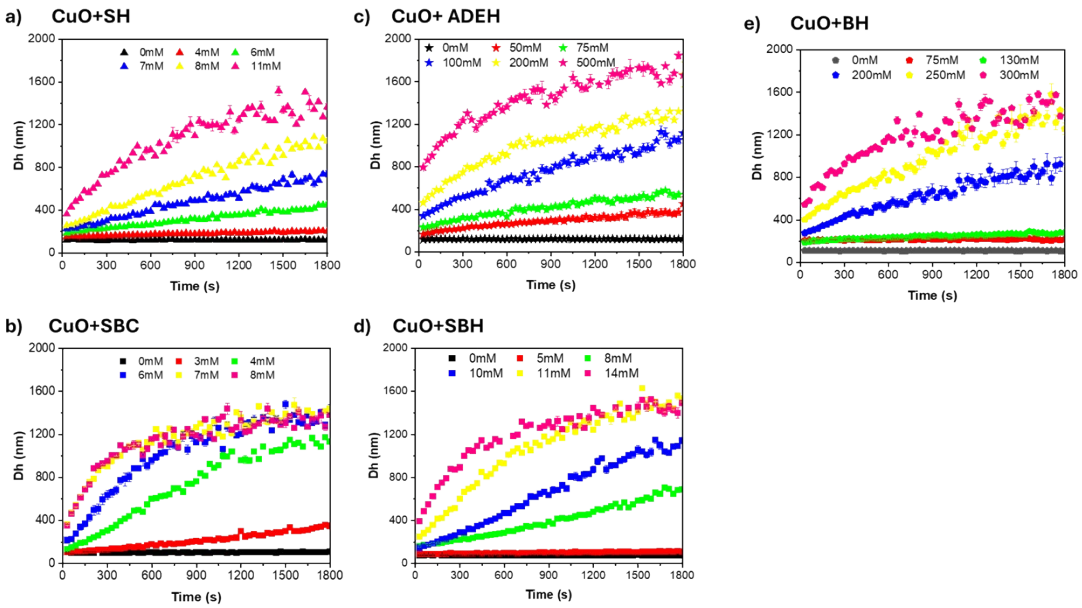

Figure S13. CuONP (100 mg L^{-1}) aggregation kinetics, as a function of NaCl concentration (0-1000 mM) at pH 5-6, in WEOM (at 5mg C L^{-1}) from a) hot-water extraction of Oxisol (SH), b) cold- and c) hot-water extraction of Oxisol-Biochar system (SBC and SBH, respectively), d) hot-water extraction of biochar (BH), and e) hot-water extraction of Amazonian Dark Earth (ADEH).

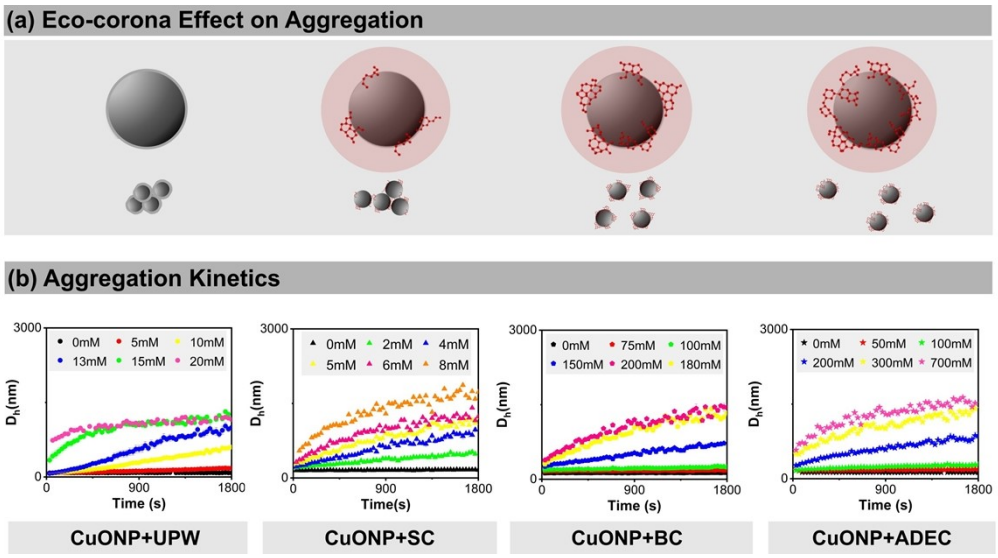

Figure S14. (a) Schematic illustration of eco-corona formation on CuONP and the resulting agglomeration behavior as influenced by eco-corona structure. (b) Aggregation kinetics of CuONP in response to increasing NaCl concentrations (0-1000 mM) at pH 5-6 across different matrices: UPW (CuONP+UPW), and WEOM extracted using cold

water from Oxisol (CuONP+SC), biochar (CuONP+BC), and Amazonian Dark Earth (CuONP+ADEC).

Nanoparticle Stability Evaluation:

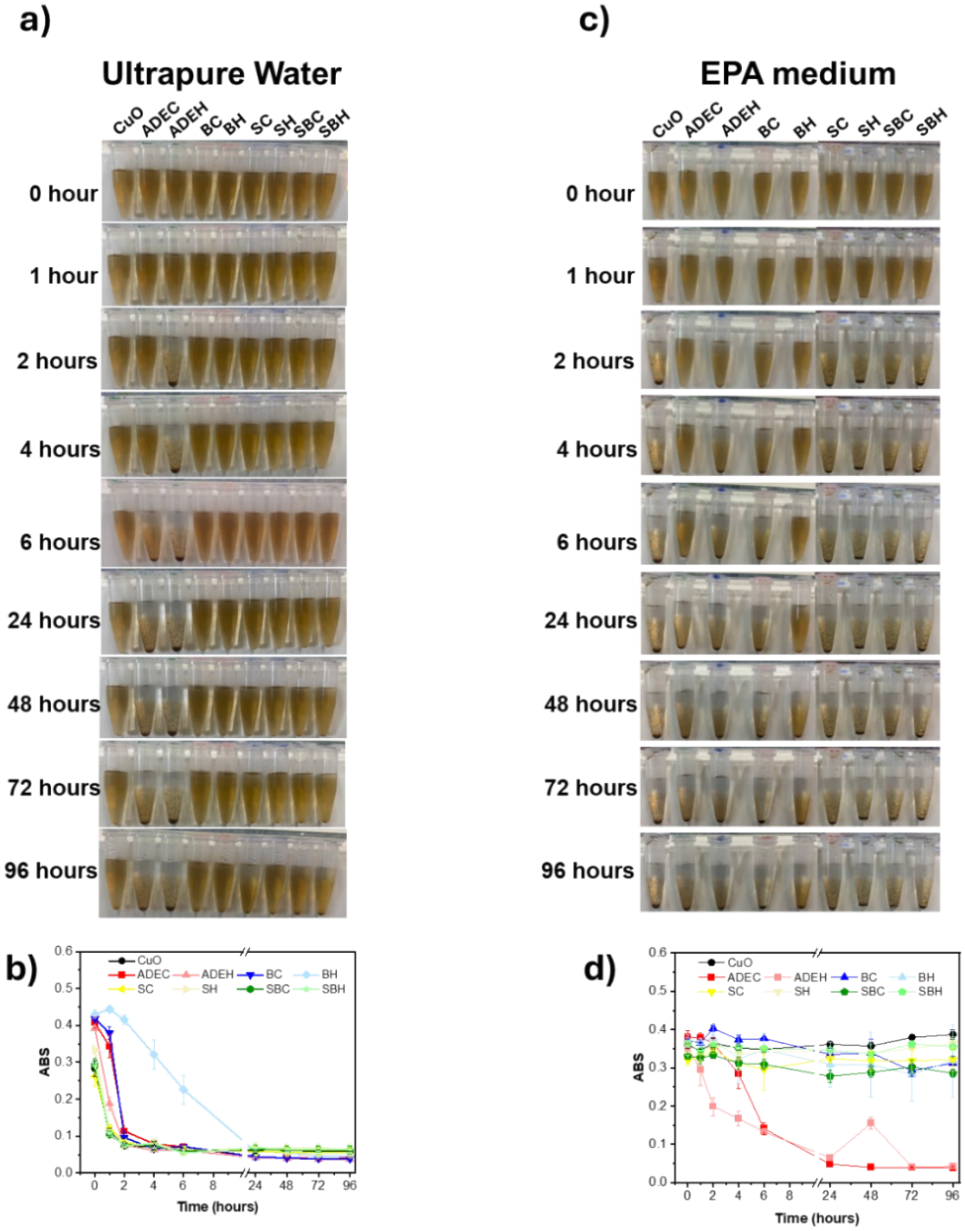

Figure S15. Photos of CuONP (100mg L^{-1}) stability at different WEOM (SC, SH, SBC, SBH, ADEC, ADEH, BC, and BH, at 5 mg C L^{-1}), evaluated over 96 hours in ultrapure water (a and b) and in EPA medium (c and d) and the corresponding absorbance measurements (396 nm).

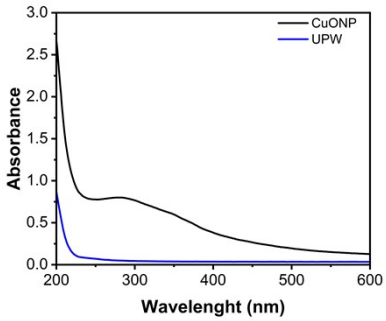

Figure S16. UV-Vis absorption spectra (200-600nm) of ultrapure water (UPW) and copper oxide nanoparticles (CuONP).

SECTION 7: Toxicity Assessment

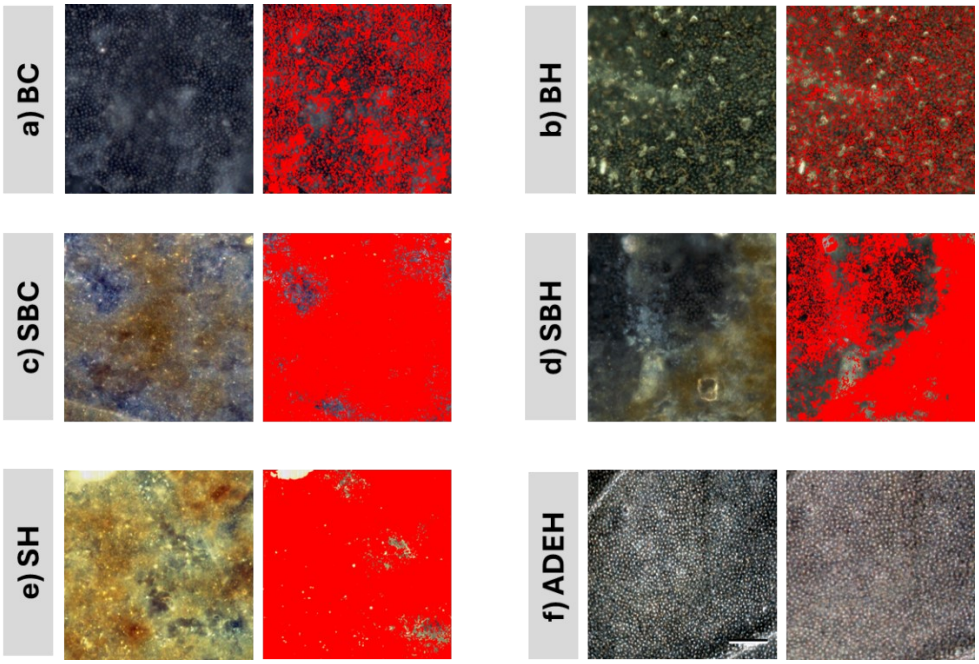

Figure S17. Hyperspectral microscopy images of the outer surface of the chorion membrane of zebrafish embryos (48 hpf) exposed to CuONP in a medium containing WEOM from biochar (BC and BH), Oxisol-Biochar system (SBC and SBH), Oxisol (SH), and Amazonian Dark Earth (ADEH).

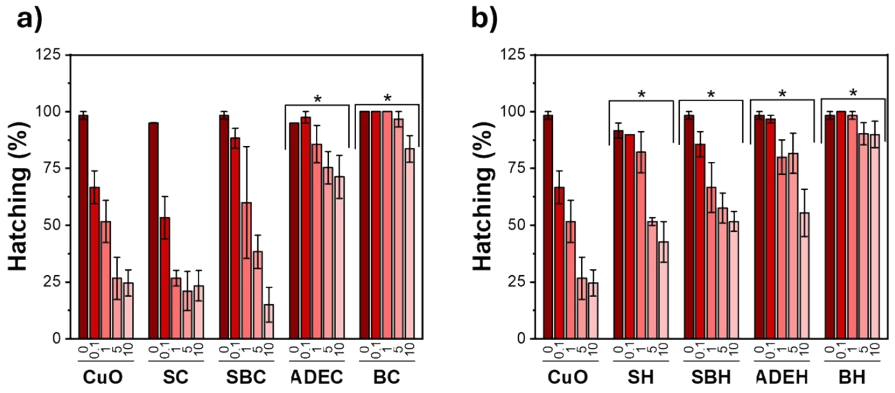

Figure S18. Hatching rate of zebrafish embryo at 96hpf exposed to CuONP and CuONP with an eco-corona formed from a) cold- and b) hot-water extractable organic carbon from Oxisol (SC and SH), Oxisol-Biochar system (SBC and SBH), Amazonian Dark Earth (ADEC and ADEH), and biochar (BC and BH) at 5 mgC/L. Data are expressed as mean ± error for three independent experiments for each concentration, and the statistical analyze was made by comparing the eco-corona treatments with the treatment containing only CuONP, where the asterisk (*) means a statistically significant difference.

Table S4. Copper oxide nanoparticles (CuONP) concentration needed to reduce 50% of the hatching rate of zebrafish embryos with 95% confidence interval.

Sample	EC_{50} ($\mu g\ L^{-1}$)	Standard Error (SE)	95% Limits
CuONP	0.69	0.27	0.11
CuONP+SC	0.24	0.08	0.07
CuONP+SH	4.96	0.76	3.31
CuONP+SBC	1.79	0.72	0.24
CuONP+SBH	>10.00	-	-
CuONP+ADEC	>10.00	-	-
CuONP+ADEH	>10.00	-	-
CuONP+BC	>10.00	-	-
CuONP+BH	>10.00	-	-

(-) Not applicable.

References

(1) Pariyar, P.; Kumari, K.; Jain, M. K.; Jadhao, P. S. Evaluation of Change in Biochar Properties Derived from Different Feedstock and Pyrolysis Temperature for Environmental and Agricultural Application. *Science of the Total Environment* **2020**, *713*. https://doi.org/10.1016/j.scitotenv.2019.136433.

(2) Fregolente, L. G.; Rodrigues, M. T.; Oliveira, N. C.; Araújo, B. S.; Nascimento, Í. V.; Souza Filho, A. G.; Paula, A. J.; Costa, M. C. G.; Mota, J. C. A.; Ferreira, O. P. Effects of Chemical Aging on Carbonaceous Materials: Stability of Water-Dispersible Colloids and Their Influence on the Aggregation of Natural-Soil Colloid. *Science of the Total Environment* **2023**, *903*. https://doi.org/10.1016/j.scitotenv.2023.166835.

(3) Liang, B.; Zhang, M.; Li, H.; Zhao, M.; Xu, P.; Deng, L. Preparation of Ceramic Foams from Ceramic Tile Polishing Waste and Fly Ash without Added Foaming Agent. *Ceram. Int.* **2021**, *47* (16), 23338–23349. https://doi.org/10.1016/j.ceramint.2021.05.047.

(4) Vieira, L. H. S. V.; Sabino, C. M. S.; Júnior, F. H. S.; Rocha, J. S.; Castro, M. O.; Alencar, R. S.; da Costa, L. S.; Viana, B. C.; de Paula, A. J.; Soares, J. M.; Filho, A. G. S.; Otubo, L.; Fechine, P. B. A.; Ghosh, A.; Ferreira, O. P. Strategic Design of Magnetic Carbonaceous Nanocomposites and Its Application as Multifunctional Adsorbent. *Carbon N. Y.* **2020**, *161*, 758–771.

(5) Fregolente, L. G.; de Castro, A. J. R.; Moreira, A. B.; Ferreira, O. P.; Bisinoti, M. C. New Proposal for Sugarcane Vinasse Treatment by Hydrothermal Carbonization: An Evaluation of Solid and Liquid Products. *J. Braz. Chem. Soc.* **2020**, *31* (1). https://doi.org/10.21577/0103-5053.20190122.

(6) Choi, J.; Oh, H.; Han, S. W.; Ahn, S.; Noh, J.; Park, J. B. Preparation and Characterization of Graphene Oxide Supported Cu, Cu2O, and CuO Nanocomposites and Their High Photocatalytic Activity for Organic Dye Molecule. *Current Applied Physics* **2017**, *17* (2), 137–145. https://doi.org/10.1016/j.cap.2016.11.020.

(7) Tahir, D.; Tougaard, S. Electronic and Optical Properties of Cu, CuO and Cu 2O Studied by Electron Spectroscopy. *Journal of Physics Condensed Matter* **2012**, *24* (17). https://doi.org/10.1088/0953-8984/24/17/175002.

(8) Zhang, F.; Zhang, W.; Wu, S.; Fu, X.; Li, S.; Yue, S. Analysis of UV–Vis Spectral Characteristics and Content Estimation of Soil DOM under Mulching Practices. *Ecol. Indic.* **2022**, *138*. https://doi.org/10.1016/j.ecolind.2022.108869.

(9) Weishaar, J. L.; Aiken, G. R.; Bergamaschi, B. A.; Fram, M. S.; Fujii, R.; Mopper, K. Evaluation of Specific Ultraviolet Absorbance as an Indicator of the Chemical Composition and Reactivity of Dissolved Organic Carbon. *Environ. Sci. Technol.* **2003**, *37* (20), 4702–4708. https://doi.org/10.1021/es030360x.

(10) Nkhili, E.; Guyot, G.; Vassal, N.; Richard, C. Extractability of Water-Soluble Soil Organic Matter as Monitored by Spectroscopic and Chromatographic Analyses. *Environmental Science and Pollution Research* **2012**, *19* (6), 2400–2407. https://doi.org/10.1007/s11356-012-0752-0.

(11) Meklesh, V.; Gentile, L.; Andersson, E.; Bhattacharya, A.; de Farias, M. A.; Cardoso, M. B.; Stålbrand, H.; Loh, W.; Škerlep, M.; Kritzberg, E.; Tunlid, A.; Olsson, U.; Persson, P. Characterization of the Colloidal Properties of Dissolved Organic Matter From Forest Soils. *Frontiers in Soil Science* **2022**, *2*. https://doi.org/10.3389/fsoil.2022.832706.

(12) Balaria, A.; Johnson, C. E. Compositional Characterization of Soil Organic Matter and Hot-Water-Extractable Organic Matter in Organic Horizons Using a Molecular Mixing Model. *J. Soils Sediments* **2013**, *13* (6), 1032–1042. https://doi.org/10.1007/s11368-013-0690-6.

(13) Curtin, D.; Beare, M. H.; Chantigny, M. H.; Greenfield, L. G. Controls on the Extractability of Soil Organic Matter in Water over the 20 to 80°C Temperature Range. *Soil Science Society of America Journal* **2011**, *75* (4), 1423–1430. https://doi.org/10.2136/sssaj2010.0401.

(14) Chantigny, M. H.; Curtin, D.; Beare, M. H.; Greenfield, L. G. Influence of Temperature on Water-Extractable Organic Matter and Ammonium Production in Mineral Soils. *Soil Science Society of America Journal* **2010**, *74* (2), 517–524. https://doi.org/10.2136/sssaj2008.0347.

(15) Chantigny, M. H.; Harrison-Kirk, T.; Curtin, D.; Beare, M. Temperature and Duration of Extraction Affect the Biochemical Composition of Soil Water-Extractable Organic Matter. *Soil Biol. Biochem.* **2014**, *75*, 161–166. https://doi.org/10.1016/j.soilbio.2014.04.011.

(16) dos Santos, J. V.; Fregolente, L. G.; Moreira, A. B.; Ferreira, O. P.; Mounier, S.; Viguier, B.; Hajjoul, H.; Bisinoti, M. C. Humic-like Acids from Hydrochars: Study of the Metal Complexation Properties Compared with Humic Acids from Anthropogenic Soils Using PARAFAC and Time-Resolved Fluorescence. *Science of the Total Environment* **2020**, *722*. https://doi.org/10.1016/j.scitotenv.2020.137815.

(17) Tadini, A. M.; Mounier, S.; Milori, D. M. B. P. Modeling the Quenching of Fluorescence from Organic Matter in Amazonian Soils. *Science of the Total Environment* **2020**, *698*. https://doi.org/10.1016/j.scitotenv.2019.134067.

(18) Sharma, P.; Laor, Y.; Raviv, M.; Medina, S.; Saadi, I.; Krasnovsky, A.; Vager, M.; Levy, G. J.; Bar-Tal, A.; Borisover, M. Compositional Characteristics of Organic Matter and

Its Water-Extractable Components across a Profile of Organically Managed Soil. *Geoderma* **2017**, *286*, 73–82. https://doi.org/10.1016/j.geoderma.2016.10.014.

(19) Chen, W.; Westerhoff, P.; Leenheer, J. A.; Booksh, K. Fluorescence Excitation-Emission Matrix Regional Integration to Quantify Spectra for Dissolved Organic Matter. *Environ. Sci. Technol.* **2003**, *37* (24), 5701–5710. https://doi.org/10.1021/es034354c.

(20) Li, B.; Li, Z.; Chen, J.; Jin, C.; Cao, W.; Peng, B. Humic-like Components in Dissolved Organic Matter Inhibit Cadmium Sequestration by Sediment. *J. Environ. Sci. (China).* **2025**, *150*, 645–656. https://doi.org/10.1016/j.jes.2024.03.055.

(21) Mielnik, L.; Kowalczuk, P. Optical Characteristic of Humic Acids from Lake Sediments by Excitation-Emission Matrix Fluorescence with PARAFAC Model. *J. Soils Sediments* **2018**, *18* (8), 2851–2862. https://doi.org/10.1007/s11368-018-1947-x.

(22) Sierra, M. M. D.; Giovanela, M.; Parlanti, E.; Soriano-Sierra, E. J. Fluorescence Fingerprint of Fulvic and Humic Acids from Varied Origins as Viewed by Single-Scan and Excitation/Emission Matrix Techniques. *Chemosphere* **2005**, *58* (6), 715–733. https://doi.org/10.1016/j.chemosphere.2004.09.038.

(23) McKnight, D. M.; Boyer, E. W.; Westerhoff, P. K.; Doran, P. T.; Kulbe, T.; Andersen, D. T. Spectrofluorometric Characterization of Dissolved Organic Matter for Indication of Precursor Organic Material and Aromaticity. *Limnol. Oceanogr.* **2001**, *46* (1), 38–48. https://doi.org/10.4319/lo.2001.46.1.0038.

(24) Zsolnay', A.; Baigar, E.; Jimenez', M.; Steinweg', B.; Saccomandi', F. Differentiating with Fluorescence Spectroscopy the Sources of Dissolved Organic Matter in Soils Subjected to Drying. *Chemosphere* **1999**, *38* (1), 45–50.

(25) Lin, Y.; Hu, E.; Sun, C.; Li, M.; Gao, L.; Fan, L. Using Fluorescence Index (FI) of Dissolved Organic Matter (DOM) to Identify Non-Point Source Pollution: The Difference in FI between Soil Extracts and Wastewater Reveals the Principle. *Science of the Total Environment* **2023**, *862*. https://doi.org/10.1016/j.scitotenv.2022.160848.

(26) Liu, C.; Li, Z.; Berhe, A. A.; Xiao, H.; Liu, L.; Wang, D.; Peng, H.; Zeng, G. Characterizing Dissolved Organic Matter in Eroded Sediments from a Loess Hilly Catchment Using Fluorescence EEM-PARAFAC and UV–Visible Absorption: Insights from Source Identification and Carbon Cycling. *Geoderma* **2019**, *334*, 37–48. https://doi.org/10.1016/j.geoderma.2018.07.029.

(27) Fan, Q.; Sun, J.; Quan, G.; Yan, J.; Gao, J.; Zou, X.; Cui, L. Insights into the Effects of Long-Term Biochar Loading on Water-Soluble Organic Matter in Soil: Implications for the Vertical Co-Migration of Heavy Metals. *Environ. Int.* **2020**, *136*. https://doi.org/10.1016/j.envint.2019.105439.

(28) Gmach, M. R.; Cherubin, M. R.; Kaiser, K.; Cerri, C. E. P. Processes That Influence Dissolved Organic Matter in the Soil: A Review. *Scientia Agricola*. Scientia Agricola 2020. https://doi.org/10.1590/1678-992x-2018-0164.

(29) Cotrufo, M. F.; Soong, J. L.; Horton, A. J.; Campbell, E. E.; Haddix, M. L.; Wall, D. H.; Parton, W. J. Formation of Soil Organic Matter via Biochemical and Physical Pathways of Litter Mass Loss. *Nat. Geosci.* **2015**, *8* (10), 776–779. https://doi.org/10.1038/ngeo2520.

(30) Novotny, E. H.; Deazevedo, E. R.; Bonagamba, T. J.; Cunha, T. J. F.; Madari, B. E.; Benites, V. D. M.; Hayes, M. H. B. Studies of the Compositions of Humic Acids from

Amazonian Dark Earth Soils. *Environ. Sci. Technol.* **2007**, *41* (2), 400–405. https://doi.org/10.1021/es060941x.

(31) Fulmer, G. R.; Miller, A. J. M.; Sherden, N. H.; Gottlieb, H. E.; Nudelman, A.; Stoltz, B. M.; Bercaw, J. E.; Goldberg, K. I. NMR Chemical Shifts of Trace Impurities: Common Laboratory Solvents, Organics, and Gases in Deuterated Solvents Relevant to the Organometallic Chemist. *Organometallics* **2010**, *29* (9), 2176–2179. https://doi.org/10.1021/om100106e.

(32) Lam, B.; Simpson, A. J. Direct 1H NMR Spectroscopy of Dissolved Organic Matter in Natural Waters. *Analyst* **2008**, *133* (2), 263–269. https://doi.org/10.1039/b713457f.

(33) Decesari, S.; Mircea, M.; Cavalli, F.; Fuzzi, S.; Moretti, F.; Tagliavini, E.; Facchini, M. C. Source Attribution of Water-Soluble Organic Aerosol by Nuclear Magnetic Resonance Spectroscopy. *Environ. Sci. Technol.* **2007**, *41* (7), 2479–2484. https://doi.org/10.1021/es0617111.

(34) Goranov, A. I.; Tadini, A. M.; Martin-Neto, L.; Bernardi, A. C. C.; Oliveira, P. P. A.; Pezzopane, J. R. M.; Milori, D. M. B. P.; Mounier, S.; Hatcher, P. G. Comparison of Sample Preparation Techniques for the (-)ESI-FT-ICR-MS Analysis of Humic and Fulvic Acids. *Environ. Sci. Technol.* **2022**, *56* (17), 12688–12701. https://doi.org/10.1021/acs.est.2c01125.

(35) Hawkes, J. A.; D'Andrilli, J.; Agar, J. N.; Barrow, M. P.; Berg, S. M.; Catalán, N.; Chen, H.; Chu, R. K.; Cole, R. B.; Dittmar, T.; Gavard, R.; Gleixner, G.; Hatcher, P. G.; He, C.; Hess, N. J.; Hutchins, R. H. S.; Ijaz, A.; Jones, H. E.; Kew, W.; Khaksari, M.; Palacio Lozano, D. C.; Lv, J.; Mazzoleni, L. R.; Noriega-Ortega, B. E.; Osterholz, H.; Radoman, N.; Remucal, C. K.; Schmitt, N. D.; Schum, S. K.; Shi, Q.; Simon, C.; Singer, G.; Sleighter, R. L.; Stubbins, A.; Thomas, M. J.; Tolic, N.; Zhang, S.; Zito, P.; Podgorski, D. C. An International Laboratory Comparison of Dissolved Organic Matter Composition by High Resolution Mass Spectrometry: Are We Getting the Same Answer? *Limnol. Oceanogr. Methods* **2020**, *18* (6), 235–258. https://doi.org/10.1002/lom3.10364.

(36) Sleighter, R. L.; Hatcher, P. G. Molecular Characterization of Dissolved Organic Matter (DOM) along a River to Ocean Transect of the Lower Chesapeake Bay by Ultrahigh Resolution Electrospray Ionization Fourier Transform Ion Cyclotron Resonance Mass Spectrometry. *Mar. Chem.* **2008**, *110* (3–4), 140–152. https://doi.org/10.1016/j.marchem.2008.04.008.

(37) Goranov, A. I.; Sleighter, R. L.; Yordanov, D. A.; Hatcher, P. G. TEnvR: MATLAB-Based Toolbox for Environmental Research. *Analytical Methods* **2023**, *15* (40), 5390–5400. https://doi.org/10.1039/d3ay00750b.

(38) Kim, S.; Kramer, R. W.; Hatcher, P. G. Graphical Method for Analysis of Ultrahigh-Resolution Broadband Mass Spectra of Natural Organic Matter, the Van Krevelen Diagram. *Anal. Chem.* **2003**, *75* (20), 5336–5344. https://doi.org/10.1021/ac034415p.

(39) Song, B.; Chen, M.; Zhao, L.; Qiu, H.; Cao, X. Physicochemical Property and Colloidal Stability of Micron- and Nano-Particle Biochar Derived from a Variety of Feedstock Sources. *Science of the Total Environment* **2019**, *661*, 685–695. https://doi.org/10.1016/j.scitotenv.2019.01.193.

(40) Fang, J.; Cheng, L.; Hameed, R.; Jin, L.; Wang, D.; Owens, G.; Lin, D. Release and Stability of Water Dispersible Biochar Colloids in Aquatic Environments: Effects of

Pyrolysis Temperature, Particle Size, and Solution Chemistry. *Environmental Pollution* **2020**, *260*, 114037. https://doi.org/10.1016/j.envpol.2020.114037.

(41) Yang, W.; Shang, J.; Sharma, P.; Li, B.; Liu, K.; Flury, M. Colloidal Stability and Aggregation Kinetics of Biochar Colloids: Effects of Pyrolysis Temperature, Cation Type, and Humic Acid Concentrations. *Science of the Total Environment* **2019**, *658*, 1306–1315. https://doi.org/10.1016/j.scitotenv.2018.12.269.